



Integrated numerical study of rainfall-induced landslides from initiation to propagation using saturation-based rheological model

R. Ghorbani, M.T. Manzari*, and A. Hajilouy-Benisi

School of Mechanical Engineering, Sharif University of Technology, Tehran, P.O. Box 11155/9567, Iran.

Received 17 April 2021; received in revised form 28 December 2021; accepted 21 February 2022

KEYWORDS

Rainfall-induced landslide;
 Slope stability;
 Saturation-based rheological model;
 Propagation;
 Initiation.

Abstract. This paper presents an integrated two-dimensional numerical framework for simulating rainfall-induced landslides from instability initiation to post-failure flow. To describe the entire process, three steps are considered in this study: (1) a coupled hydro-stability analysis which detects the failure plane using the Finite Element Method (FEM) (pre-failure stage); (2) computing the local rheology of the failed mass (wet sandy soil) based on the water saturation at the onset of failure using the saturation-based rheological model (transition stage); and (3) a continuum-based propagation analysis which solves the flow of the wet material employing the Smoothed Particle Hydrodynamics (SPH) method (post-failure stage). Finally, to investigate the influence of rheological model on the post-failure behavior, the computed final deposition profile and flow kinetic energy are compared with those of a viscoplastic model.

© 2022 Sharif University of Technology. All rights reserved.

1. Introduction

Slope failures and debris flows triggered by intense rainfall are devastating natural hazards that occur frequently all around the world. Integrated modeling of such landslides from initiation of instability to post-failure flow-like motion remains a challenge. At present, only a few studies have addressed the entire process of rainfall-induced landslide in a single numerical framework [1–3]. The seepage-stress coupling and stress-strain modeling of the wet soil are the main difficulties in the integrated modeling [2].

Literatures pertinent to rainfall-induced landslides are classified into two main categories [4]: (1)

the pre-failure stage [5,6] and (2) the post-failure stage studies [7,8]. The pre-failure stage includes seepage and slope stability analysis which determines the time and the location of landslide, while the post-failure stage deals with debris flow and its propagation.

In the pre-failure stage, at each step of infiltration, the seepage analysis determines pore water pressure distribution, while the stability analysis assesses the stability of the slope considering the effect of pore water pressure. The possible failure plane is detected by defining the factor of safety (F_S) as the ratio of the available local shear strength to the minimum local shear stress required to maintain equilibrium [9]. When F_S for a surface falls below one, its location is considered as the failure surface. The Limit Equilibrium Methods (LEM) are the most commonly used methods for this purpose. They divide the soil mass into vertical slices and calculate the factor of safety by applying the principle of moments and/or

*. Corresponding author. Tel.: +98 21 66165689
 E-mail address: mtmanzari@sharif.edu (M.T. Manzari)

force equilibrium [10,11]. The LEM is computationally convenient to use, but it only satisfies the equations of statics and does not consider strain and displacement compatibility. Alternatively, one can use Finite Element Method (FEM) analysis to obtain the stress field and evaluate the stability of the soil. Although this approach is computationally more expensive, it can provide detailed information about the status of the slope [11,12]. The effects of soil parameters (angle of internal friction and cohesion) [13] as well as soil suction and ground water table [14] on the stability of soil slope have been previously investigated. Some studies have analyzed the influence of spatial variability, such as heterogeneity and discontinuity within the granular assembly, on the failure behavior [15,16]. To examine the influence of local failure on global failure, the effect of microstructural instability on the macroscopic failure has been studied using a multi-scale approach [17].

Due to the large deformation, the traditional Lagrangian FEM is not optimal for numerical modeling of the post-failure motion [18]. Instead, meshless or particle-based methods, such as Smoothed Particle Hydrodynamic (SPH) method [19], Discrete Element Method (DEM) [20], Material Point Method (MPM) [21], and hybrid Finite/Discrete Element Method (FDEM) [22] have been successfully used to simulate the propagation. When particle-based methods are used, the particle-water interaction (e.g., drag and buoyancy forces) is modeled using a flow solver coupled with the particle phase solver. These methods solve a single-phase flow system first and then, apply the hydrodynamic forces on the moving particles. A commonly used approach blends the DEM with a flow solver [23,24]. Despite their capabilities, the computational efficiency remains a challenge in these methods [25]. On the other hand, the continuum-based methods need a rheological model to determine the behavior of the material. This is a major challenge for continuum-based methods and choosing the most appropriate rheological model for wet granular flow is still a matter of debate. For example, Mast et al. [26] compared the hardening-softening Matsuoka-Nakai model with the Drucker-Prager model and found that the final deposition profile was affected by the choice of the model. Fern and Soga [27] used Mohr-Coulomb and Nor-Sand models for simulating the collapse of a granular mass and demonstrated that the energy dissipation was dependent on the rheological model. Ceccato and Simonini [28] applied Mohr-Coulomb failure criterion with an elastic perfectly plastic model and Drucker-Prager yielding condition with a viscoplastic model and showed that using different models yielded different results in the impact forces and destruction potential of a granular flow.

In almost all of the few continuum-based studies performed on the integrated modeling of rainfall-

induced landslides [3,29], the same failure criterion (Mohr-Coulomb) is used for both pre-failure and post-failure stages and the soil behavior is often described by a Mohr-Coulomb strain-softening model based on Bishop's effective stress [3]. However, the variation in soil rheological behavior induced by rainfall infiltration and its variation with water saturation was not considered in the propagation stage. This exhibits a missing link between the two stages and can lead to noticeable errors in the computed results (e.g., landslide velocity and runout). Using a saturation-based rheological model can lead to a better connection between pre-failure and post-failure stages.

The rheology of wet granular materials has been studied experimentally [30], numerically using discrete simulation [30], and by multiscale modeling based on thermodynamic principles [31]. In these studies, the liquid distribution and inter-particle forces are described in terms of liquid bridges and capillary forces between grains, respectively. The pendular liquid bridge model [32] is commonly used in weakly wetted conditions. However, for simulating the flow of landslides, determining the rheological behavior as a function of saturation is essential. In their recent study [33], the authors proposed a power law rheological model for simulating the flow of wet granular materials over a wide range of saturations. The rheological model was a function of inertial number (I) and saturation. The inertia number is defined as $\dot{\gamma}d_p/\sqrt{\sigma/\rho_p}$, where $\dot{\gamma}$ is the shear rate, d_p and ρ_p are the diameter and density of soil particles, and σ is the normal stress. This saturation-based rheological model can be used as a transition stage to determine the local rheology of wet soil at the onset of failure based on its saturation distribution.

To describe the entire process of rainfall-induced landslides, this paper presents an integrated model based on a three-step (pre-failure, transition, and post-failure) strategy. We start with water saturation at the onset of failure, compute the local rheology of the wet soil based on the saturation, and then solve the flow of wet material using a continuum-based method. The pre-failure results (seepage analysis and slope failure detection) are benchmarked against experimental and numerical studies from the literature. The rheological model (transition stage) was previously verified in [33] for the dry soil and the results were reported for soils with different degrees of saturation. In the present paper, the rheological model is verified for the saturated soil and then, used for propagation modeling.

2. Computational procedure

In this study, the coupled hydro-stability FE analysis, the saturation-based rheological model, and the propa-

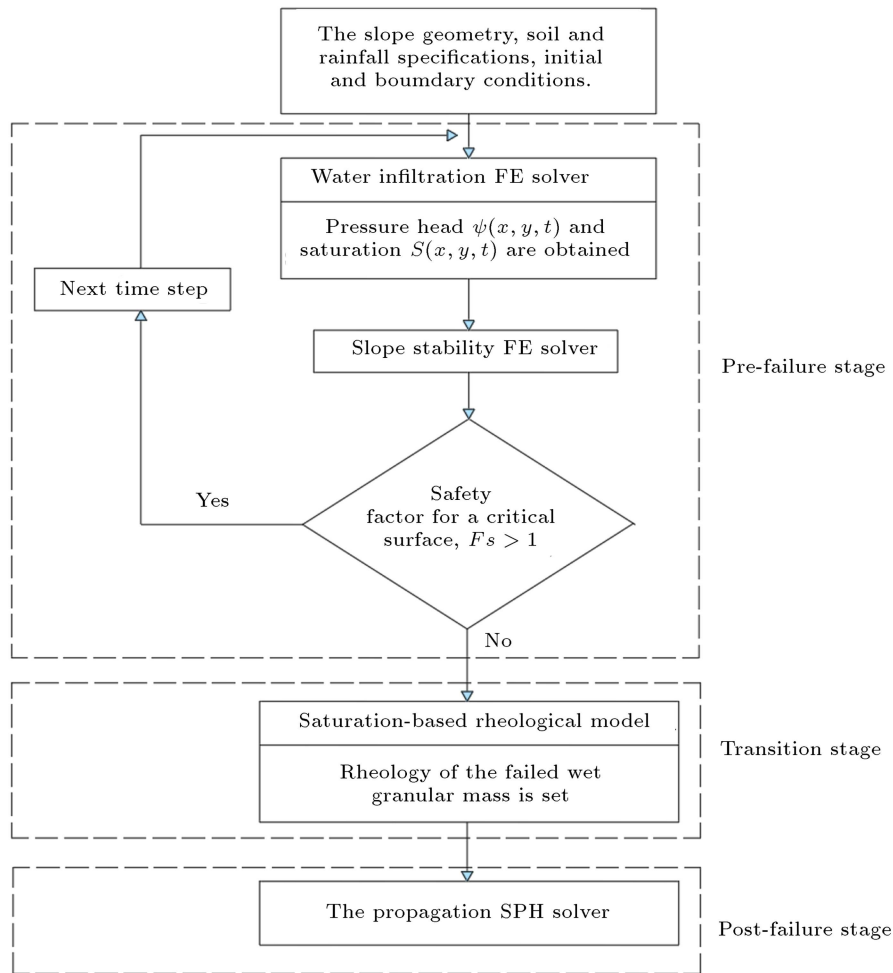


Figure 1. The flowchart of the current integrated numerical simulation.

gation SPH solver are integrated to simulate the entire process of rainfall-induced landslides. The flowchart of the simulation procedure is shown in Figure 1, and the mathematical formulations are described as follows.

2.1. Step 1: Pre-failure stage

Equations governing rainfall infiltration and slope stability analysis are described in this section.

2.1.1. Hydrological model

Considering the soil as a rigid isotropic porous medium, the unsteady Darcian flow of water in a variably saturated soil is mathematically described by Richards' equation [34] (in 2D form):

$$\frac{\partial \theta(\psi)}{\partial t} = \frac{\partial}{\partial x} \left[K(\psi) \frac{\partial \psi}{\partial x} \right] + \frac{\partial}{\partial y} \left[K(\psi) \left(\frac{\partial \psi}{\partial y} - 1 \right) \right], \quad (1)$$

where the flow of air is neglected due to large mobility contrast between the air and water [35]. In Eq. (1), θ is the non-dimensional volumetric water content [$L^3 L^{-3}$], ψ the pressure head [L], x the horizontal spatial coordinate [L], y the vertical spatial coordinate

taken as positive downward [L], and K the hydraulic conductivity [LT^{-1}].

$\theta(\psi)$ and $K(\psi)$ are highly nonlinear functions, in general [35]. A number of empirical correlations have been proposed for these functions [36,37]. In this study, $\theta(\psi)$ and $K(\psi)$ proposed by van Genuchten [38] are used. These models use the statistical pore-size distribution model of Mualem [39]. The van Genuchten models are given by [38]:

$$\theta(\psi) = \begin{cases} \theta_r + \frac{\theta_s - \theta_r}{(1 + |\alpha \psi|^n)^J} & \psi < 0 \\ \theta_s & \psi \geq 0 \end{cases}, \quad (2)$$

$$K(\psi) = K_s \cdot S^l \cdot [1 - (1 - S^{1/J})^2], \quad (3)$$

where:

$$S = \frac{\theta(\psi) - \theta_r}{\theta_s - \theta_r}, \quad (4)$$

$$J = 1 - \frac{1}{n}, \quad n > 1, \quad (5)$$

where θ_r and θ_s denote the residual and saturated wa-

ter contents, respectively; K_s is the saturated hydraulic conductivity, α the inverse of the air-entry value (or bubbling pressure), n a pore-size distribution index, and l a pore-connectivity parameter. Eqs. (2) to (5) contain six independent parameters: θ_r , θ_s , α , n , K_s , and l [39]. l is set to 0.5 in the current simulation [31].

The initial pressure head and water content in the domain Ω are:

$$\psi(x, y, t) = \psi_0(x, y), \quad (6)$$

and:

$$\theta(x, y, t) = \theta_0(x, y), \quad (7)$$

where ψ_0 and θ_0 are known functions.

The model can deal with pressure head and flux boundary conditions. Head boundary conditions are given by:

$$\psi(x, y, t) = B_1(x, y, t) \quad \text{for } (x, y) \in \Omega_{B_1}, \quad (8)$$

and flux boundary conditions are of the following form:

$$K \left(\frac{\partial \psi}{\partial x} \right) = B_2(x, y, t) \quad \text{for } (x, y) \in \Omega_{B_2}, \quad (9)$$

$$K \left(\frac{\partial \psi}{\partial y} - 1 \right) = B_3(x, y, t) \quad \text{for } (x, y) \in \Omega_{B_3}, \quad (10)$$

where Ω_{B_1} , Ω_{B_2} , and Ω_{B_3} indicate head and flux type boundary segments and $B_1[L]$, $B_2[LT^{-1}]$ and $B_3[LT^{-1}]$ are prescribed functions. In this study, the flux condition is used for boundaries with no fluxes (B_2 and B_3 are set to zero) and for boundaries on which precipitation occurs (B_3 is set to be the rainfall intensity function).

Flux boundaries are controlled by atmospheric conditions for soil-air interfaces. For such boundaries, if the applied flux is larger than the soil saturated hydraulic conductivity (K_s), the flux boundary condition switches to the head boundary condition. In fact, this atmospheric boundary condition removes the excess water resulting from oversaturation as surface runoff from the surface [40]. Due to the temporal scale of the flow processes in this study, the current model ignores the evaporation and transpiration [41].

The governing differential equation (Eq. (1)) is solved using the standard Galerkin finite elements along with the backward Euler time integration scheme as outlined in [35,42].

$\psi(x, y, t)$ and $S(x, y, t)$ are the outputs of the hydrological analysis. According to the Bishop's equation, the total stress (σ) must be replaced by the effective stress (σ') in partially saturated soils. So, the calculated pore water pressure distribution can affect the stability of the soil mass. The next step is to examine the stability of the soil slope at each time step of infiltration.

2.1.2. Slope stability model

In this study, the finite element Shear Strength Reduction (SSR) method [12] based on the Mohr-Coulomb failure criterion is used for detecting the failure plane. The SSR method defines the factor of safety (F_S) as the ratio of the real shear strength to the minimum shear strength required for failure prevention. In this technique, the shear strength parameters are changed until the failure conditions are met. The reduced shear strength parameters \bar{c} and $\bar{\zeta}$ are given by [12]:

$$\bar{c} = \frac{c}{\text{SRF}}, \quad (11)$$

$$\bar{\zeta} = \arctan \left(\frac{\tan \zeta}{\text{SRF}} \right), \quad (12)$$

where c and ζ are the cohesion and the friction angle of the granular material, respectively, and SRF is the strength reduction factor. The value of SRF that corresponds to the slope failure is equal to the factor of safety (F_S) [12]. In this study, the non-convergence criterion [12] is applied to detect the failure plane. By increasing the values of the SRF, the algorithm gradually weakens the soil parameters until the iteration limit is reached without convergence. This actually means that no stress distribution can be achieved to satisfy both the global equilibrium and failure criterion. This condition causes a sharp increase in the nodal displacements inside the mesh and it is implied that the failure has occurred.

2.2. Step 2: Transition stage (the saturation-based rheological model)

In their recent study [33], the authors proposed a saturation-based rheological model for simulating the flow of wet granular materials. In [33], the DEM has been employed to establish a rheological model that correlates the apparent viscosity of a granular material to shear rate, normal stress, and water saturation. A power law rheological model was devised as follows:

$$\mu = A(S) \times I^{-B(S)}, \quad (13)$$

where A and B values are listed in Table 1. In Eq. (13), μ is the apparent viscosity [Pa.s] and I is the inertia number defined as $I = \frac{\dot{\gamma} d_p}{\sqrt{\sigma/\rho_p}}$, where d_p and ρ_p are the diameter and density of soil particles, σ is the normal stress [Pa], and $\dot{\gamma}$ is the shear rate.

Table 1. Coefficients of the rheological equation for different saturations [33].

Parameter	Park's numerical simulation [44]	Current numerical simulation
l	0.452	0.452
α	3.6	0.59
n	1.189	6.93

For a soil subjected to the rainfall infiltration, it has been shown that up to a critical degree of saturation, the apparent viscosity increases with saturation [33]. However, when the saturation exceeds this critical value, the apparent viscosity drops below the viscosity of dry soil. For a homogenous soil composed of mono-sized spherical particles with a cubic lattice initial particle arrangement, the critical saturation was calculated to be 34.2% [33]. The details of derivation of the rheological model (Eq. (13)) can be found in [33]. In this study, the transition stage is modeled by applying Eq. (13) along with Table 1.

2.3. Step 3: Post-failure stage (the propagation model)

In this section, the SPH method [43] is used for studying the flow of wet granular materials. This study considers the flowing material as an incompressible fluid and utilizes the saturation-based rheological model to determine the behavior of the wet material. To capture the realistic behavior of granular materials, a slip boundary condition is also imposed on the solid boundaries [19].

In the present study, it is assumed that change in the bulk density of the material is not significant during flow. Accordingly, the continuity and momentum for the equivalent fluid are:

$$\nabla \cdot \vec{V} = 0, \quad (14)$$

$$\frac{D\vec{V}}{Dt} = -\frac{1}{\rho_b} \nabla P + \frac{1}{\rho_b} \nabla \cdot \tau + \vec{g}, \quad (15)$$

where ρ_b is the bulk density, P the pressure of fluid,

\vec{V} the velocity vector, \vec{g} the gravitational acceleration vector, and τ the stress tensor, which is determined using the saturation-based rheological model. The bulk density of the wet material is obtained as:

$$\rho_b = (1 - \kappa)\rho_p + \kappa S\rho_{water}, \quad (16)$$

where κ is the porosity of material and ρ_{water} is the density of water. A detailed description of solving Eqs. (14) and (15) using the SPH method can be found in [19].

In this paper, an in-house flow solver named SePeHr [19] is used. This code has been recently used for modeling the collapse of two-dimensional dry granular material using a visco-plastic rheology on horizontal rigid and entrainable beds [19].

3. Results

The test case presented by Park in [44] was chosen as a benchmark for this study. Park presented both experimental data and numerical results in his paper. In his experiments, Park measured the water content and soil suction (negative pore water pressure) changes due to artificial rainfall at four locations within a slope composed of frictional non-cohesive initially dry sand. The location of the failure plane was also reported and then, the experimental observations were compared with numerical results. Figure 2 schematically shows Park's experimental setup and Table 2 shows the material properties used in his experiment. The parameters of van Genuchten model considered in the current numerical analysis are presented in Table 3. The current parameters obtained based on the measured

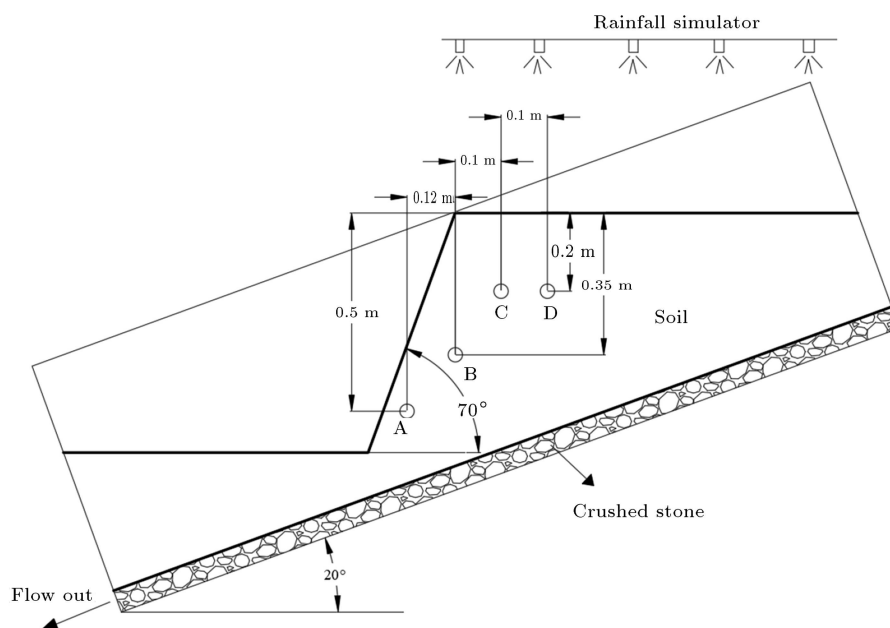


Figure 2. Schematic of the case study considered for validation of the infiltration model. A, B, C, and D are the locations of water content and soil suction sensors.

Table 2. Physical properties of the materials in Park's experiments [44].

Coefficient	Saturation degree			
	10%	20%	30%	$s \geq 34.2\%$
A	9e-4	4.2e-4	1.3e-4	0.17
B	2.39	2.58	2.84	0.85

Table 3. Parameters of van Genuchten model.

Material	Parameter	Value
Soil	K_S (m/s)	1.3×10^{-4}
	θ_s	0.38
	θ_r	0.05
	Density (kg/m ³)	1605
	Cohesion (kPa)	0
	Friction angle (°)	33.6
Crushed stone	K_S (m/s)	0.13
	Density (kg/m ³)	1900
	Cohesion (kPa)	0
	Friction angle (°)	45

soil suctions and volumetric water contents [44] are more consistent with experimental data in comparison to the values considered by Park. The soil sits on top of a 5 cm drainage layer made of crushed stones and the rainfall intensity is 30 mm/h in the experiments.

The current results are divided into four parts: validation of the hydrological (Section 3.1), the slope stability (Section 3.2), the rheological model (Section 3.3), and simulation of the propagation of the wet collapsed material (Section 3.4).

3.1. Seepage results

The computational grid consists of 3777 triangular elements and 2005 nodes, as shown in Figure 3, and the boundary conditions are imposed, as shown in Figure 4. The initial condition is set based on

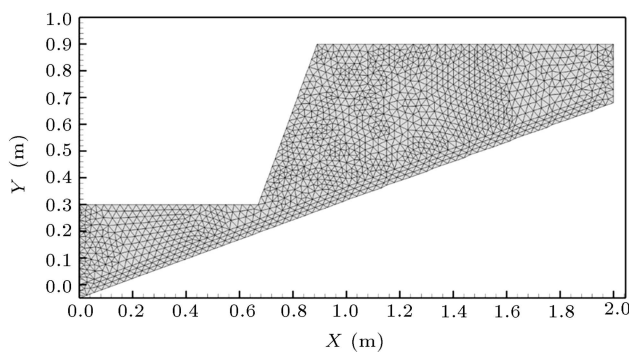


Figure 3. The geometry and mesh of the current computational domain.

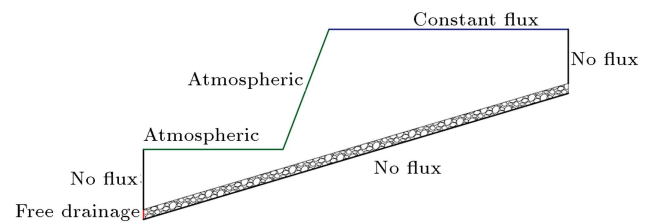


Figure 4. Boundary conditions for Park's benchmark problem.

the measured porewater pressures before the onset of rainfall ($\theta(x, y) = 0.05$ at $t = 0$) [44].

Figure 5 shows the contours of volumetric water content for different time steps after the onset of rainfall. In accordance with the study in [44], the rainfall starts after measuring the initial water content. As can be observed, when the water reaches the crushed stone layer due to the higher hydraulic conductivity, it starts moving faster and eventually leaves the soil from the free drainage boundary. The crushed stone layer was formed to ensure that slope failure occurred only when there was a change in the shear strength of the slope due to rainfall seepage; therefore, the influence of the water table rising was eliminated (the maximum saturation in the domain is about 99.5%).

Figures 6 and 7 compare the results of the current numerical simulation with experimental and numerical results of Park [44] at point C in Figure 2. As can be seen, the current numerical results are closer to the experimental data. A possible reason for the differences in the numerical results is the definition of hydraulic functions in van Genuchten model.

3.2. Slope stability results

Figure 8 compares the experimental and numerical results of Park [44] with the result of the current numerical analysis in the prediction of the failure plane. As can be seen, the current result is closer to the experimental observation than to Park's numerical analysis.

In the experimental results, the failure time, i.e., the time when the factor of safety falls below 1, has been reported. Park [44] analyzed the failure time experimentally and the changes in F_S numerically. Figure 9 compares the results obtained in the present study with those presented in [44]. As shown in the figure, ten minutes after the onset of rainfall ($t = 190$ min), the factor of safety began decreasing. In the current study, F_S fell below one at $t = 325$ min, meaning that the failure occurred after 145 minutes from the onset of rainfall. In the Park's experiment and numerical analysis, the failure happened 140 and 130 minutes after the rainfall onset, respectively. Thus, the current simulation predicts the time of failure more accurately. More accurate simulation of water infiltration and use of the FE stability analysis, instead of the LEM method, can be mentioned as the reasons for this improvement.

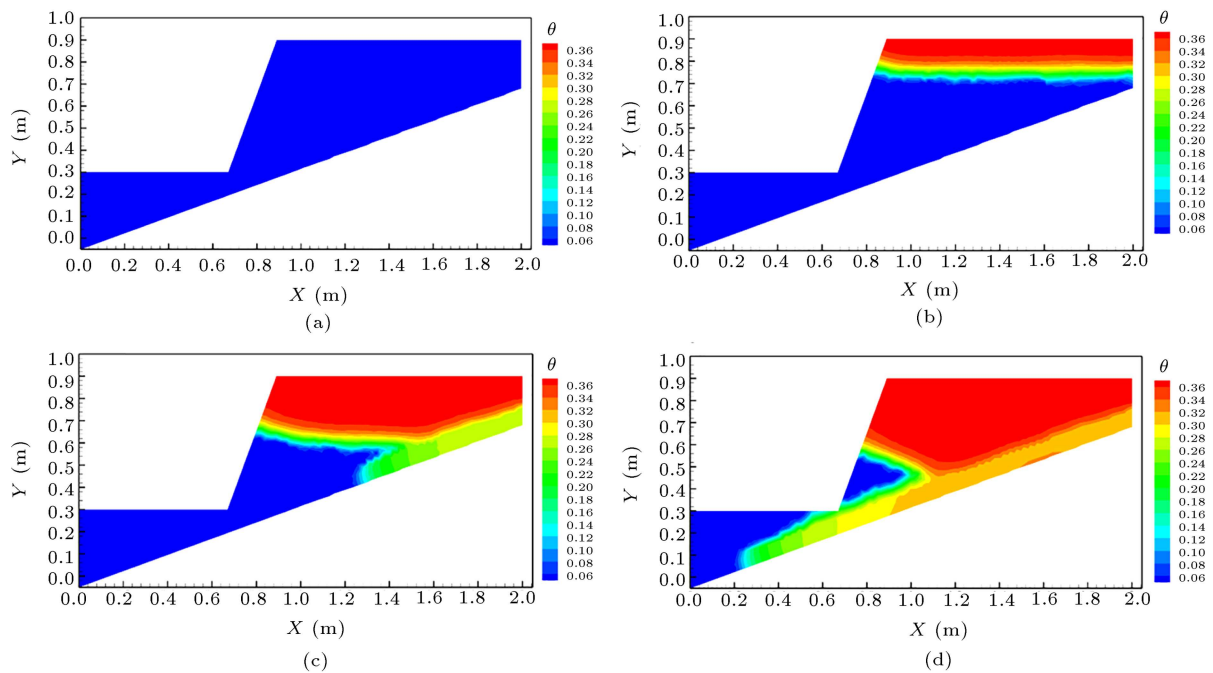


Figure 5. Contours of volumetric water content at different times after the onset of rainfall: (a) $t = 180$ min, (b) $t = 220$ min, (c) $t = 260$ min, and (d) $t = 300$ min. Rainfall starts at $t = 180$ min.

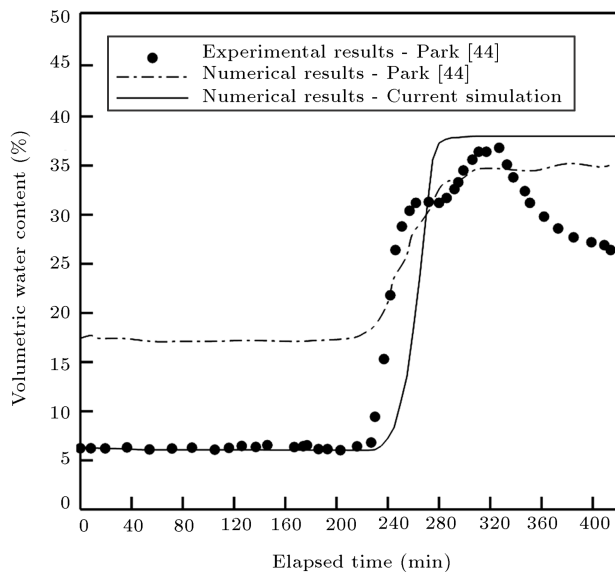


Figure 6. Comparison of the water content results in the current simulation with the experimental and numerical results of Park at point C in the slope. Rainfall starts at $t = 180$ min.

3.3. Verification of the saturated rheological model

According to Figure 8, the slope failure occurred in the saturated zone. Therefore, only the saturated state of the rheological model (Section 2.3) must be included in the propagation model. In [33], the rheological model was verified for the sand in dry state and the results were reported for the wet sands at different

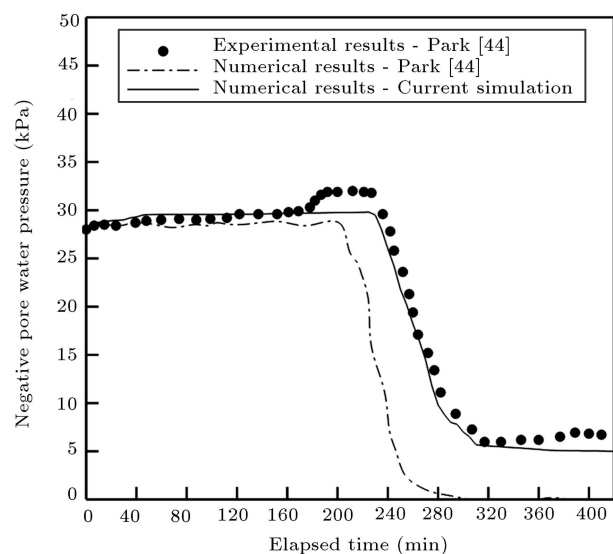


Figure 7. Comparison of the negative pore water pressure results in the current simulation with the experimental and numerical results of Park at point C in the slope. Rainfall starts at $t = 180$ min.

saturation. Before using the rheological model at the post-failure stage, this section verifies the model in predicting the behavior of the saturated sand. To this end, the saturated rheological equation (Section 2.2) was implemented into the SePeHr [19] code and the validity of the rheological model was examined by comparing the simulation with experimental results. To conduct this verification, the collapse of a fully-

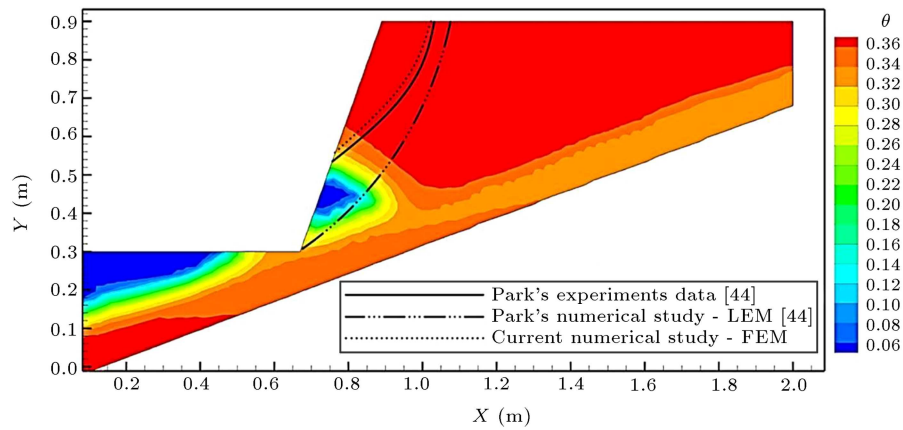


Figure 8. Comparison of the observed failure plane in the Park's experiment and the predicted failure plane in Park's and current numerical simulations.

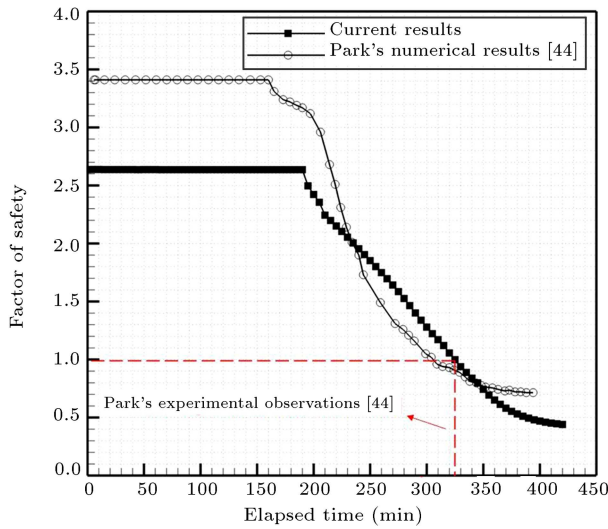


Figure 9. Factor of safety versus time obtained in this work and those presented by Park [44].

Table 4. Specimen specifications in the experiments conducted by Cessato et al. [45].

Specification	Value
Grains mean diameter (d_p)	$2.5 \cdot 10^{-3}$ m
Grain density (ρ_p)	2625 kg/m^3
Initial porosity (κ)	0.4
Cohesion (c)	0 Pa
Angle of internal friction (ζ)	35°

saturated granular material on a horizontal rigid bed is compared with the experimental results obtained by Ceccato et al. [45]. Figure 10 schematically shows the case studied in this section and the properties of the sand are listed in Table 4. The base and lateral walls are made of glass and the gate is made of plexiglass. The details of sand preparation and test were outlined in [45].

One of the most important indicators of collapses

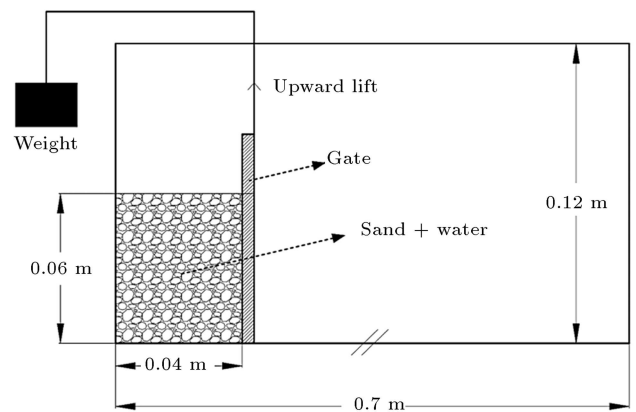


Figure 10. Schematic of the case study considered for verification of the rheological model.

is the distance traveled by the moving material, called “runout”, denoted here by X_∞ . In the current numerical simulation, the slip length was modified to obtain runout values close to the experiments. A value $l_s = 0.009$ for the slip length gave the best match with the experimental data.

The shape of the collapsed material is compared with the experimental results at different times in Figure 11. According to the results, current numerical simulations are in close agreement with the experimental data.

The assumption that the material bulk density remains constant during the collapse can be a reason why the results do not completely match. The top part desaturation during collapse is another phenomenon that the current simulation has not captured.

3.4. Propagation results

The final step of this study is the propagation simulation. By assigning the saturated rheology to the flowing material, it is possible to simulate the propagation of the saturated soil. Figure 12 shows the simulation of the post-failure flow in which the SPH particles

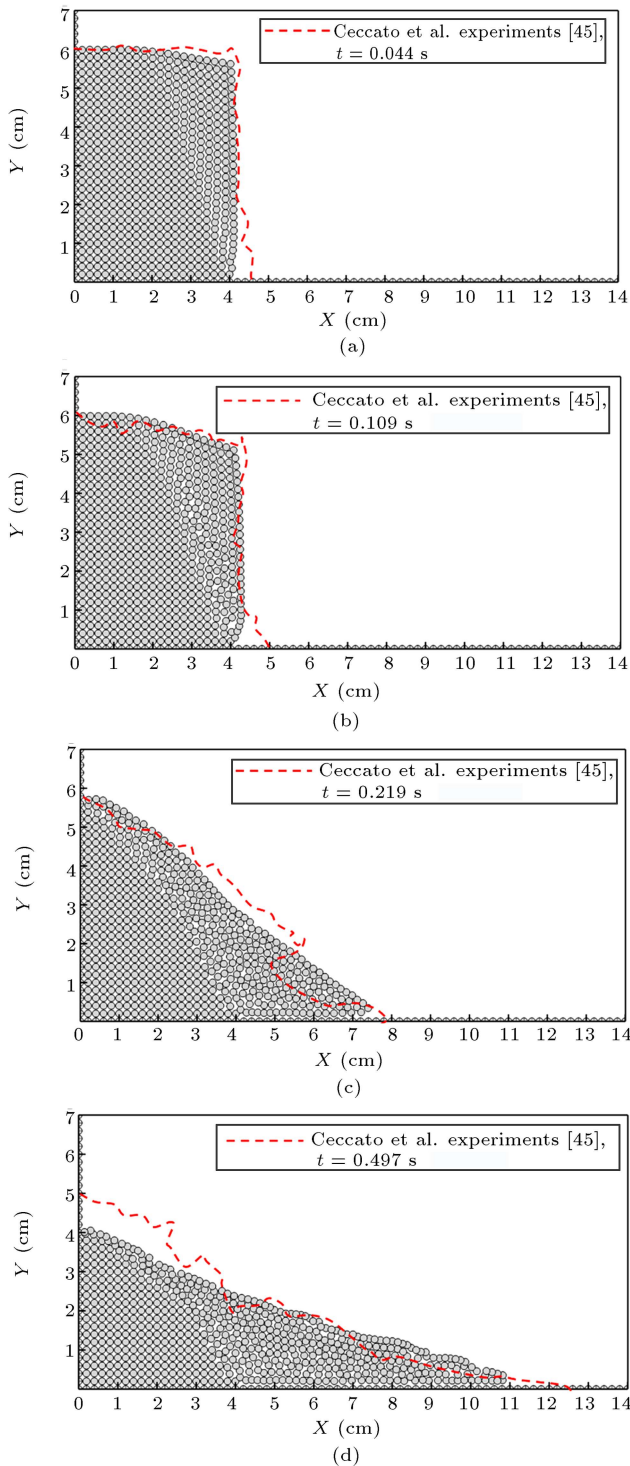


Figure 11. Comparison of the free surface obtained by numerical simulation with experimental results [45] at different simulation times: (a) $t = 0.044$ s, (b) $t = 0.109$ s, (c) $t = 0.219$ s, and (d) $t = 0.497$ s.

are colored based on their velocity magnitude. As illustrated in Figure 12, the propagation stops at $t = 1.65$ s.

In order to investigate the influence of the rheological model on the post-failure motion, the propaga-

tion simulation is repeated with a modified Bingham viscoplastic rheology (bi-viscous model) that does not consider the effect of saturation. This model reads [19]:

$$\tau = \begin{cases} M\mu_B\dot{\gamma} & \text{if } |\dot{\gamma}| < \frac{\tau_y}{M\mu_B} \\ \tau_y + \mu_B(\dot{\gamma} - \frac{\tau_y}{M\mu_B}) & \text{if } |\dot{\gamma}| \geq \frac{\tau_y}{M\mu_B} \end{cases} \quad (17)$$

where μ_B is the Bingham viscosity and M is the viscosity factor of order 10^4 [19].

Figure 13 shows the final deposition profile for both simulations. As can be seen, the computed runout distance is longer when using the saturation-based rheology.

To compare the flow destructive potential, the kinetic energy of the flow is considered as a criterion. The Kinetic Energy (KE) at each time step is computed as [19]:

$$KE = \sum_{i=1}^N m_i \frac{V_i^2}{2}, \quad (18)$$

where m_i , V_i , and N are the mass, the velocity, and the total number of the SPH particles.

Figure 14 shows the variations of the kinetic energy of the flow with time for the two different rheologies. As shown in the figure, the destructive potential is higher when a saturation-based rheological model is used.

4. Conclusion

In this paper, an integrated numerical framework based on a three-step strategy was presented for simulating rainfall-induced landslides from the initiation of instability to the debris flow. The main results of the present study are summarized as follows:

- In the pre-failure stage, the progressive changes in the pore pressure, volumetric water content, and F_S during water infiltration can be evaluated. To make a better connection between pre-failure and post-failure stages, a transition stage is proposed which uses the saturation-based rheological model to compute the local rheology of the failed mass based on its saturation. The main advantages of the current integrated framework include nonexistence of pre-assumed failed mass and considering the variation in the soil rheological behavior induced by rainfall infiltration in the propagation stage;
- The entire landslide process was simulated for a soil slope exposed to rainfall and the results were presented. As demonstrated by the results, considering the effect of the water saturation on the soil rheological behavior can affect the propagation results. The current simulation that used the saturation-based rheological model predicted different deposition profiles with higher runout and higher flow

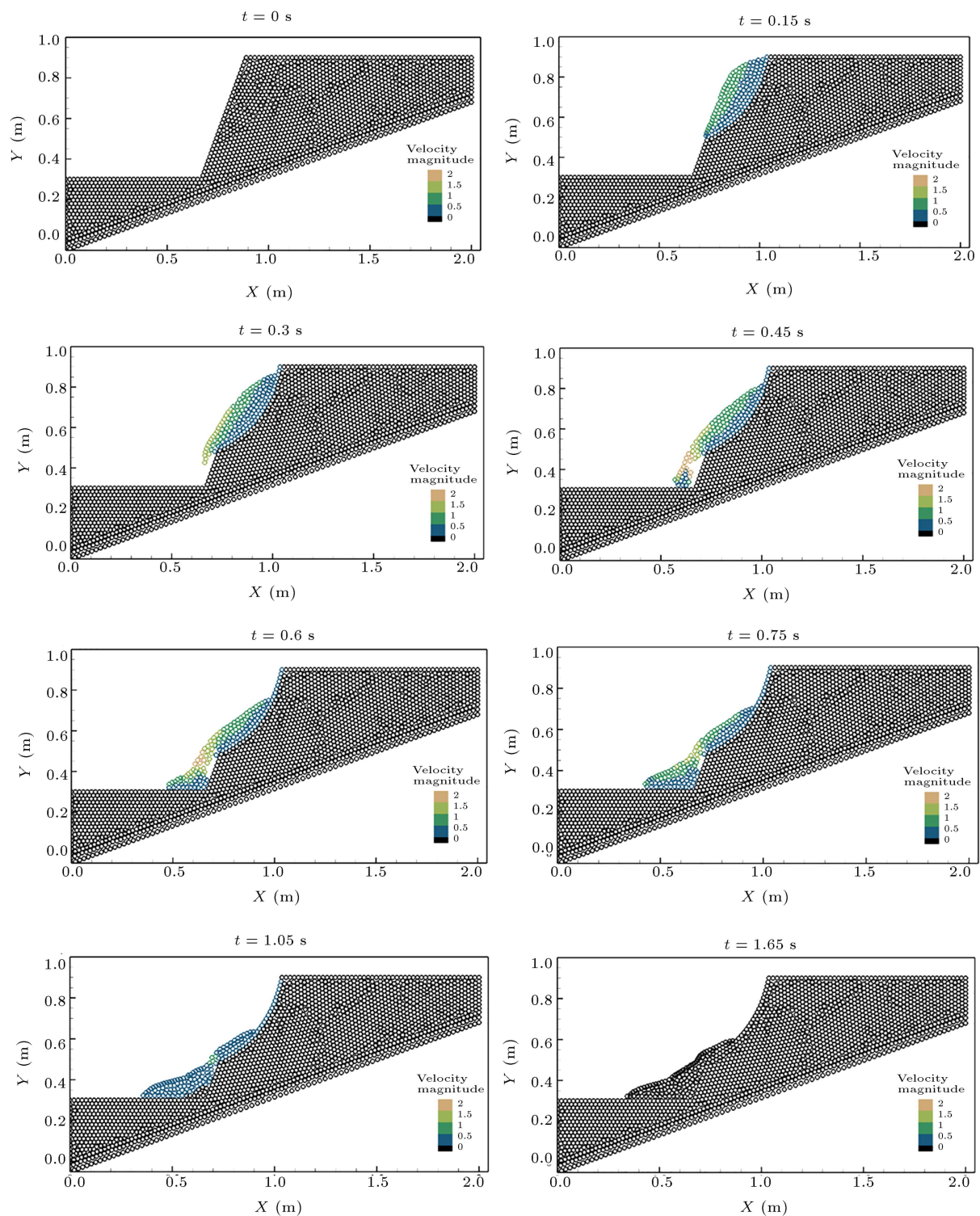


Figure 12. Post failure simulation of the debris flow based on the saturation-based rheology.

kinetic energy than simulations using a visco-plastic rheology.

This study proposed a numerical procedure for integrated simulation of rainfall-induced landslides. This research is subject to some limitations: (1) The

computational domain was two-dimensional; (2) The bed was rigid and non-entrainable; and (3) In the rheological model, the granular soil was assumed to be a homogenous assembly of mono-sized spherical particles which initially formed a cubic lattice packing. Despite these considerations, no other physical restric-

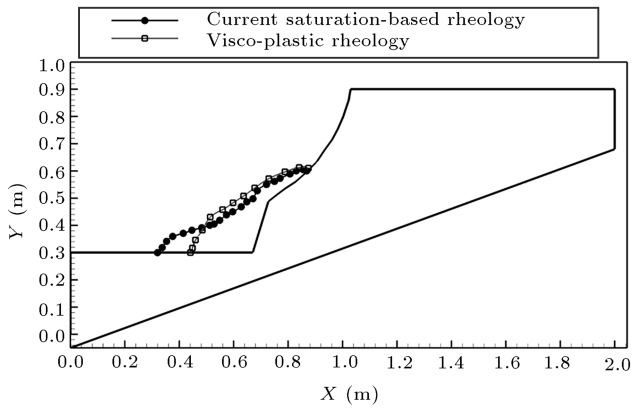


Figure 13. Comparison of the deposition profiles obtained by the saturation-based and modified Bingham rheology.

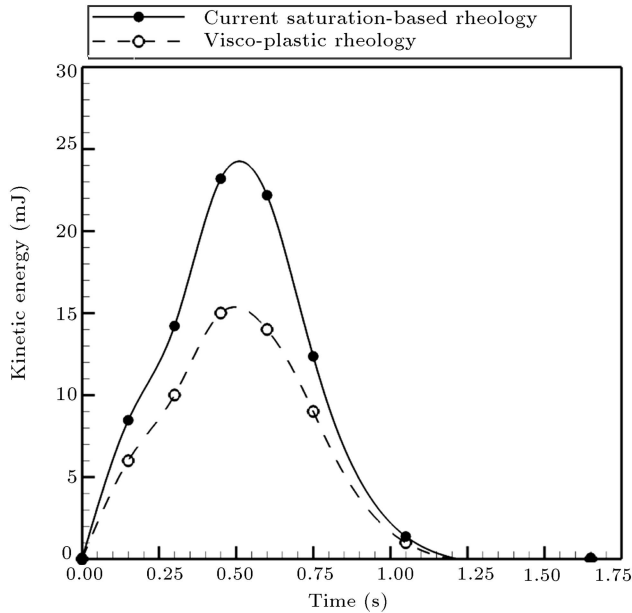


Figure 14. Variations of the kinetic energy of the flow with time for both simulations.

tion is foreseen to limit the application of the present procedure.

Nomenclature

F_S	Factor of safety
τ	Shear stress
$\dot{\gamma}$	Shear rate
μ	Apparent viscosity
I	Inertia number
d_p	Particle diameter
ρ_p	Particle density
ρ_b	Bulk density
ρ_{water}	Water density
σ	Normal stress

σ'	Effective stress
ψ	Pressure head
ξ	Angle of internal friction
$\bar{\xi}$	Reduced angle of internal friction
c	Cohesion
\bar{c}	Reduced cohesion
SRF	Shear Reduction Factor
P	Pressure of fluid
S	Saturation degree
θ	Volumetric water content
θ_r	Residual volumetric water content
θ_s	Saturated volumetric water content
g	Gravitational acceleration
m	Mass
V	Velocity
t	Time
x	Horizontal spatial coordinate
y	Vertical spatial coordinate
K	Hydraulic conductivity
K_S	Saturated hydraulic conductivity
α	Inverse of air-entry value
n	Pore size distribution index
l	Pore connectivity parameter
κ	Porosity
l_s	Slip length
μ_B	Bingham viscosity
M	Viscosity factor
KE	Kinetic Energy
N	Total number of SPH particles

References

- Wang, B., Vardon, P., and Hicks, M. "Rainfall-induced slope collapse with coupled material point method", *Engineering Geology*, **239**, pp. 1–12 (2018).
- Shen, P., Zhang, L., Chen, H., et al. "EDDA 2.0: integrated simulation of debris flow initiation and dynamics considering two initiation mechanisms", *Geoscientific Model Development*, **11**, pp. 2841–2856 (2018).
- Chen, X., Zhang, L., Zhang, L., et al. "Modelling rainfall-induced landslides from initiation of instability to post-failure", *Computers and Geotechnics*, **129**, p. 103877 (2021).
- Cascini, L., Cuomo, S., Pastor, M., et al. "Modeling of rainfall-induced shallow landslides of the flow-type", *Journal of Geotechnical and Geoenvironmental Engineering*, **136**, pp. 85–98 (2010).
- Gallage, C., Abeykoon, T., and Uchimura, T. "Instrumented model slopes to investigate the effects of slope inclination on rainfall-induced landslides", *Soils and Foundations*, **61**, pp. 160–174 (2021).

6. Marin, R., and Velásquez, M. “Influence of hydraulic properties on physically modelling slope stability and the definition of rainfall thresholds for shallow landslides”, *Geomorphology*, **351**, p. 106976 (2020).
7. Manenti, S., Amicarelli, S., Palazzolo, N., et al. “Post-failure dynamics of rainfall-induced landslide in oltrepavese”, *Water*, **12**, p. 2555 (2020).
8. Hungr, O. “A model for the runout analysis of rapid flow slides, debris flows, and avalanches”, *Canadian Geotechnical Journal*, **32**, pp. 610–623 (1995).
9. Abramson, L., *Slope Stability and Stabilization Methods*, 2nd Ed., New York: Wiley (1996).
10. Liu, S., Shao, L., and Li, H. “Slope stability analysis using the limit equilibrium method and two finite element methods”, *Computers and Geotechnics*, **63**, pp. 291–298 (2015).
11. Duncan, J. “State of the art: Limit equilibrium and finite-element analysis of slopes”, *Journal of Geotechnical Engineering*, **122**, pp. 577–596 (1996).
12. Griffiths, D. and Lane, P. “Slope stability analysis by finite elements”, *Géotechnique*, **49**, pp. 387–403 (1999).
13. Sharma, A., Raju, P., Sreedhar, V., et al. “Slope stability analysis of steep-reinforced soil slopes using finite element method”, *Geotechnical Applications*, **13**, pp. 163–171 (2019).
14. Ho, I., Li, S., and Ma, L. “Analysis of partially saturated clayey slopes using finite element method”, *Soil Mechanics and Foundation Engineering*, **56**, pp. 382–389 (2020).
15. Xie, F., Liu, C., Zhao, T., et al. “Slope stability analysis via discrete element method and Monte Carlo simulations”, *IOP Conference Series: Earth and Environmental Science*, **861**, p. 032023 (2021).
16. Zhang, W., Meng, F., Chen, F., et al. “Effects of spatial variability of weak layer and seismic randomness on rock slope stability and reliability analysis”, *Soil Dynamics and Earthquake Engineering*, **146**, p. 106735 (2021).
17. Zhao, C., Yin, Z., and Hicher, P. “A multiscale approach for investigating the effect of microstructural instability on global failure in granular materials”, *International Journal for Numerical and Analytical Methods in Geomechanics*, **42**, pp. 2065–2094 (2018).
18. Beuth, L., Benz, T., Vermeer, P., et al. “Large deformation analysis using a quasi-static material point method”, *Journal of Theoretical and Applied Mechanics*, **38**, pp. 45–60 (2008).
19. Nikooei, M. and Manzari, M. “Studying effect of entrainment on dynamics of debris flows using numerical simulation”, *Computers & Geosciences*, **134**, p. 104337 (2020).
20. Lu, C., Tang, C., Chan, Y., et al. “Forecasting landslide hazard by the 3D discrete element method: A case study of the unstable slope in the Lushan hot spring district, central Taiwan”, *Engineering Geology*, **183**, pp. 14–30 (2014).
21. Yamaguchi, Y., Takase, S., Moriguchi, S., et al. “Solid-liquid coupled material point method for simulation of ground collapse with fluidization”, *Computational Particle Mechanics*, **7**, pp. 209–223 (2019).
22. Guo, N. and Zhao, J. “A coupled FEM/DEM approach for hierarchical multiscale modelling of granular media”, *International Journal for Numerical Methods in Engineering*, **99**, pp. 789–818 (2014).
23. Li, X. and Zhao, J. “A unified CFD-DEM approach for modeling of debris flow impacts on flexible barriers”, *International Journal for Numerical and Analytical Methods in Geomechanics*, **42**, pp. 1643–1670 (2018).
24. Liu, W. and Wu, C. “Modelling Complex Particle-Fluid Flow with a Discrete Element Method Coupled with Lattice Boltzmann Methods (DEM-LBM)”, *Chem Engineering*, **4**, p. 55 (2020).
25. Zhao, T., Dai, F., and Xu, N. “Coupled DEM-CFD investigation on the formation of landslide dams in narrow rivers”, *Landslides*, **14**, pp. 189–201 (2016).
26. Mast, C., Arduino, P., Mackenzie-Helnwein, P., et al. “Simulating granular column collapse using the material point method”, *Acta Geotechnica*, **10**, pp. 101–116 (2014).
27. Fern, E. and Soga, K. “The role of constitutive models in MPM simulations of granular column collapses”, *Acta Geotechnica*, **11**, pp. 659–678 (2016).
28. Ceccato, F. and Simonini, P. “Granular flow impact forces on protection structures: MPM numerical simulations with different constitutive models”, *Procedia Engineering*, **158**, pp. 164–169 (2016).
29. Wang, D., Li, L., and Li, Z. “A regularized Lagrangian meshfree method for rainfall infiltration triggered slope failure analysis”, *Engineering Analysis with Boundary Elements*, **42**, pp. 51–59 (2014).
30. Schwarze, R., Gladkyy, A., Uhlig, F., et al. “Rheology of weakly wetted granular materials: a comparison of experimental and numerical data”, *Granular Matter*, **15**, pp. 455–465 (2013).
31. Zhao, C., Salami, Y., Hicher, P., et al. “Multiscale modeling of unsaturated granular materials based on thermodynamic principles”, *Continuum Mechanics and Thermodynamics*, **31**, pp. 341–359 (2018).
32. Willett, C., Adams, M., Johnson, S., et al. “Capillary bridges between two spherical bodies”, *Langmuir*, **16**, pp. 9396–9405 (2000).
33. Ghorbani, R., Manzari, M., and Hajilouy-Benisi, A. “Development of a saturation-based $\mu(I)$ -rheology for wet granular materials using discrete element method”, *Scientia Iranica*, **28**, pp. 2719–2732 (2021).

34. Bogaard, T. and Greco, R. “Landslide hydrology: from hydrology to pore pressure”, *WIREs Water*, **3**, pp. 439–459 (2015).
35. Farthing, M. and Ogden, F. “Numerical solution of Richards’ equation: A review of advances and challenges”, *Soil Science Society of America Journal*, **81**, pp. 1257–1269 (2017).
36. van Genuchten, M. and Pachepsky, Y. “Hydraulic properties of unsaturated soils”, *Encyclopedia of Earth Sciences Series*, Springer, pp. 368–376 (2011).
37. Guellouz, L., Askri, B., Jaffré, J., et al. “Estimation of the soil hydraulic properties from field data by solving an inverse problem”, *Scientific Reports*, **10**, p. 9359 (2020).
38. van Genuchten, M. “A closed-form equation for predicting the hydraulic conductivity of unsaturated soils”, *Soil Science Society of America Journal*, **44**, pp. 892–898 (1980).
39. Mualem, Y. “A new model for predicting the hydraulic conductivity of unsaturated porous media”, *Water Resources Research*, **12**, pp. 513–522 (1976).
40. Shanmugam, M., Kumar, G., Narasimhan, B., et al. “Effective saturation-based weighting for interblock hydraulic conductivity in unsaturated zone soil water flow modelling using one-dimensional vertical finite-difference model”, *Journal of Hydroinformatics*, **22**, pp. 423–439 (2019).
41. Zhang, G., *Modelling Hydrological Response at the Catchment Scale*, Eburon Academic Publishers, p. 145 (2007).
42. List, F. and Radu, F. “A study on iterative methods for solving Richards’ equation”, *Computational Geosciences*, **20**, pp. 341–353 (2016).
43. Hashemi, M., Fatehi, R., and Manzari, M. “A modified SPH method for simulating motion of rigid bodies in Newtonian fluid flows”, *International Journal of Non-Linear Mechanics*, **47**, pp. 626–638 (2012).
44. Park, M. “Behavior analysis by model slope experiment of artificial rainfall”, *Natural Hazards and Earth System Sciences*, **16**, pp. 789–800 (2016).
45. Ceccato, F., Leonardi, A., Girardi, V., et al. “Numerical and experimental investigation of saturated granular column collapse in air”, *Soils and Foundations*, **60**, pp. 683–696 (2020).

Biographies

Ramin Ghorbani received his BS (2012) and MS degrees (2014) in Mechanical Engineering with a minor in Energy Conversion. He is currently a PhD candidate at Sharif University of Technology. His researches are focused on the numerical modeling and simulation of granular flows.

Mehrdad T. Manzari received his PhD degree from the University of Wales Swansea in 1996. He has been a Professor of Mechanical Engineering at Sharif University of Technology since 2010. He was the Director of Thermo-Fluid Group (2007–2009), Director of Center of Excellence in Energy Conversion (2007–2009), and Director of Graduate Studies (2005–2007) at the School of Mechanical Engineering of Sharif University of Technology. His research interests are multiphase flows in porous media with applications in hydrocarbon reservoirs, simulation of fluid flow and heat transfer in manufacturing processes, fluid flow and heat transfer in micro-electro-mechanical-systems, non-Newtonian fluid flows, computational methods in engineering, and smoothed particle hydrodynamics with engineering applications.

Ali Hajilouy-Benisi received his PhD degree at the Mechanical Engineering Department of Imperial College at the University of London in 1993. He was a faculty member of the Institute of Water and Energy and since 1978, has been a faculty member at the School of Mechanical Engineering at Sharif University of Technology. He served as the Director of the Fluid Mechanics Lab (1993–1995), Founder and Director of the Turbocharger Lab (1993), Turbocharging lab (2000), and Gas Turbine Lab (2008) at the School of Mechanical Engineering of Sharif University of Technology. His research interests are experimental and theoretical investigations of turbochargers, turbocharging, and gas turbines.